

# Continuous generation of an ultracold atomic beam using crossed moving optical lattices

Shoichi Okaba<sup>1,2</sup>, Ryoto Takeuchi<sup>1,3</sup>, Shigenori Tsuji<sup>2,4</sup>, and Hidetoshi Katori<sup>1,2,3,\*</sup>

<sup>1</sup>*Department of Applied Physics, Graduate School of Engineering, The University of Tokyo, Bunkyo-ku, Tokyo 113-8656, Japan*

<sup>2</sup>*Space-Time Engineering Research Team, RIKEN Center for Advanced Photonics, Wako, Saitama 351-0198, Japan*

<sup>3</sup>*Quantum Metrology Laboratory, RIKEN, Wako, Saitama 351-0198, Japan*

<sup>4</sup>*JEOL Ltd., Akishima, Tokyo 196-8558, Japan*

(Received 20 December 2023; revised 25 January 2024; accepted 8 February 2024; published 5 March 2024)

Using orthogonally crossed moving lattices, we demonstrate the continuous transport of  $^{88}\text{Sr}$  atoms in the long-lived metastable  $^3P_0$  and  $^3P_2$  states to a region free from scattered laser-cooling light, while two-stage cooling on the  $^1S_0$ - $^1P_1$  and  $^3P_2$ - $^3D_3$  transitions is being conducted. The transfer efficiency between the crossed lattices was close to unity when laser cooling was applied in the crossed region. For a clock laser propagating along the lattice axis, such a lattice-trapped atomic beam enables continuous interrogation of the clock transition free from the Doppler effect arising from the thermal motion of atoms.

DOI: 10.1103/PhysRevApplied.21.034006

## I. INTRODUCTION

Ultracold neutral atoms play a pivotal role in quantum computation [1,2], simulation [3–6], atomic clocks [7–10], and interferometers [11–15], which rely on well-defined quantum states of a large number of atoms with a long coherence time. While the laser cooling of atoms serves as an indispensable ingredient in these endeavors, simultaneous application of laser cooling has been avoided as it significantly perturbs the quantum states under investigation and degrades the atomic coherence.

Consequently, the laser cooling and the quantum state operations are applied sequentially in time. This introduces a dead time between successive measurements for atomic clocks and interferometers, which gives rise to the Dick-effect noise [16] in addition to the quantum projection noise [17]. Repetition of such measurements improves the instability as  $\tau^{-1/2}$  for an averaging time  $\tau$  [16]. In contrast, zero-dead-time (ZDT) operation may quickly improve the instability as  $\tau^{-1}$ . This motivates the realization of ZDT operation by combining two Cs atomic clocks [18] and two optical lattice clocks [10].

An atomic beam allows continuous interrogation of atoms with probe fields incident from the transverse direction, as employed for Cs beam clocks [19], optical Ramsey spectrometers, and atom interferometers [12,13,20]. To extend the atom-probe interaction time, a laser-cooled

atomic beam was developed for atomic clocks [21] and interferometers [22], where the major challenge is to prevent atoms under interrogation from scattered laser-cooling photons.

By spatially separating the cooling steps, a continuous Bose-Einstein condensation (BEC) has been demonstrated [23], where the key idea was to allocate the condensate outside the line of sight of cooling lasers by transporting atoms with an optical dipole guide [24,25]. Magnetic guides [26–28], moving magnetic traps [29,30], optical tweezers [1,2,31], and hollow-core fibers [32,33] offer nondissipative guides for atoms. Among them, a moving optical lattice [34,35] allows transporting atoms confined in the Lamb-Dicke regime (LDR), where atoms can be interrogated free from the Doppler shift arising from their thermal motion [36] for a probe laser incident along the lattice axis. On the other hand, by employing long-lived metastable states [37,38], multiple cooling steps can be conducted simultaneously in the same location [39–41].

We report continuous generation of an ultracold strontium beam in the  $5s5p$   $^3P_0$  and  $^3P_2$  metastable states while laser cooling on the  $5s^2$   $^1S_0$ - $5s5p$   $^1P_1$  and  $5s5p$   $^3P_2$ - $5s4d$   $^3D_3$  transitions is being conducted [41]. In particular, we demonstrated a crossed moving lattice to guide the atoms to an orthogonal moving lattice [42], where atoms can be free from scattered photons in laser cooling. This allows for continuous operation of clocks [43] and interferometers. We investigated transfer efficiency in the crossed moving lattice for atoms in the

\*katori@amo.t.u-tokyo.ac.jp

$^1S_0$  ground state, and  $^3P_0$  and  $^3P_2$  metastable states. We observed that the transfer efficiency approached unity by applying laser cooling in the crossed region. The experimental results were in reasonable agreement with classical trajectory simulations. The scheme can be extended to the other isotopes, such as  $^{87}\text{Sr}$ , to conduct longitudinal spectroscopy, where atoms confined in the LDR interact with a probe laser illuminated longitudinally to the atomic beam [43].

## II. EXPERIMENTAL SETUP

### A. Two-stage cooling using the metastable state

Figure 1(a) shows the schematic of our experiment based on the two-stage laser cooling reported in Ref. [41]. The  $^{88}\text{Sr}$  atoms are magneto-optically cooled and trapped on the  $5s^2\ ^1S_0$ – $5s5p\ ^1P_1$  transition at 461 nm. During the magneto-optical trapping (MOT), atoms relax to the  $5s5p\ ^3P_2$  state via the  $5s4d\ ^1D_2$  state and are magnetically trapped by the same quadrupole magnetic field as used for the MOT [44]. Relevant energy levels are given in Fig. 1(c). The magnetically trapped atoms are cooled

on the  $5s5p\ ^3P_2(m_J = 2)$ – $5s4d\ ^3D_3(m_J = 3)$  transition at  $\lambda_{\text{IR}} = 2.92 \mu\text{m}$  [37,38]. An infrared (IR) cooling laser is applied downward ( $-y$ ) and is blue-detuned by  $\approx 5$  MHz from the resonance with an intensity of  $I_{\text{IR}} \sim 6 \times 10^2 I_0$ , with  $I_0 = 0.3 \mu\text{W/cm}^2$  being the saturation intensity of the transition [41]. The equilibrium position of the laser-cooled atoms is given by the magnetic trapping force, gravity, and radiation pressure of the IR laser, which is located 5 mm below the center of the quadrupole magnetic field. We set a moving optical lattice near the equilibrium position to load and transport the atoms. The typical vacuum pressure was  $1 \times 10^{-7} \text{ Pa}$ .

### B. Moving lattice in a ring cavity

The moving optical lattice with a Rayleigh range of 55 mm is formed inside a power-buildup bowtie cavity. The two moving lattices orthogonally intersect at  $x = y = 0$ , as shown in Fig. 1(a). Two lattice lasers at  $\lambda_L = 813 \text{ nm}$ , each with a power of 300 mW, are coupled to the ring cavity modes in the clockwise and counterclockwise directions, with frequencies  $v_L^{\text{cw}}$  and  $v_L^{\text{ccw}}$ . The frequency difference  $\Delta v = v_L^{\text{ccw}} - v_L^{\text{cw}}$  determines the velocity  $v_L = \lambda_L \Delta v / 2$  of

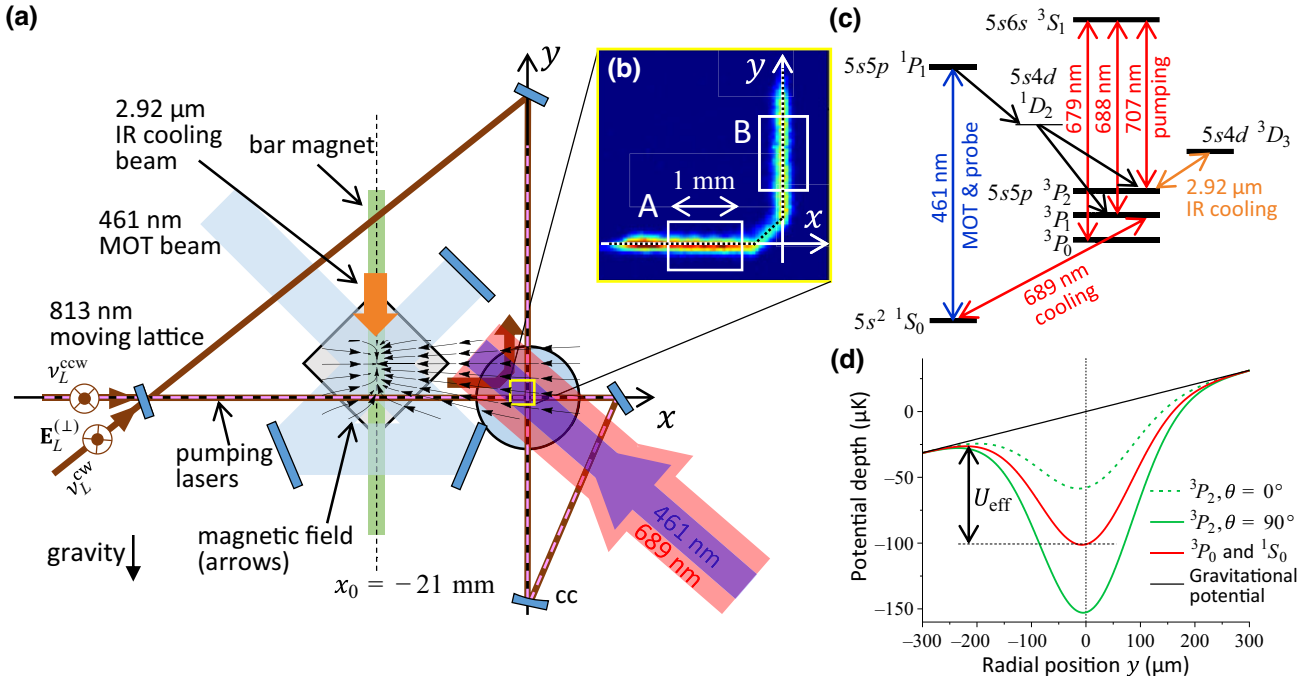


FIG. 1. Experimental platform. (a) Magneto-optical trapping (MOT) of  $^{88}\text{Sr}$  on the  $^1S_0$ – $^1P_1$  transition continuously populates the  $^3P_2$  metastable state. Atoms in the  $^3P_2$  metastable state are trapped by a quadrupole magnetic field created by a 50-mm-long permanent magnet (light-green line) and a coil (not shown). A cooling laser at 461 nm (light blue) is used for the MOT. An IR cooling laser at  $2.92 \mu\text{m}$  (orange) cools the magnetically trapped atoms on the  $^3P_2$ – $^3D_3$  transition. Ultracold atoms cooled by the IR cooling transition are loaded into a moving optical lattice (brown lines) formed inside a bowtie cavity. After traveling 21 mm in the  $+x$  direction, the atoms are redirected to the  $+y$  direction by the crossed moving lattice. A probe laser at 461 nm and a cooling laser at 689 nm illuminate the intersection of the moving lattices (thick lines in purple and red). (b) An image of atoms covers the area of  $3.5 \times 3.5 \text{ mm}^2$  at the intersection. (c) Relevant energy levels for Sr. Pumping lasers at 679, 688, and 707 nm are superimposed on the  $x$  lattice as shown by the pink dashed line in (a). (d) Gravito-optical potential along the  $y$  direction at the atom loading position  $x_0 = -21 \text{ mm}$ . Effective trap depths are dependent on the electronic states and the lattice polarization  $\theta$  (see main text).

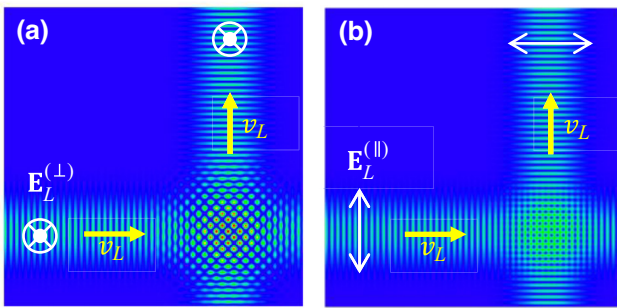


FIG. 2. (a) Lattice intensity distribution for the lattice laser polarization  $\mathbf{E}_L^{(\perp)}$  perpendicular to the cavity plane. The lattice periods are exaggerated for visibility. Interference of two orthogonal moving lattices guides the atoms with the velocity  $\mathbf{v} = (v_L, v_L)$ . (b) For the lattice laser polarization  $\mathbf{E}_L^{(\parallel)}$  parallel to the cavity plane, the lattice depth is given by the sum of the orthogonal lattices.

the moving lattice. The lattice laser polarization can be perpendicular,  $\mathbf{E}_L^{(\perp)}$ , or parallel,  $\mathbf{E}_L^{(\parallel)}$ , to the cavity plane ( $z = 0$ ), as shown in Fig. 2. In the former case, interference of two moving lattice fields at the intersection creates four times deeper lattice potential than that created by the  $x$  or  $y$  lattice, which facilitates the guiding of atoms following the local minima of moving lattice potentials, as discussed later.

The ring cavity consists of three flat mirrors and a concave (cc) mirror with a radius of 150 mm. The power enhancement by the cavity is about 77. The cavity is stabilized to one of the lattice lasers by using a piezo-electric transducer attached to one of the cavity mirrors. The  $e^{-2}$  beam radius of the cavity mode diverges from  $w_0 = 169 \mu\text{m}$  at the loading position  $x_0 = -21 \text{ mm}$  to  $w_1 = 203 \mu\text{m}$  at  $x = 0$ , where the  $x$  lattice crosses with the  $y$  lattice with the radius of  $w_2 = 228 \mu\text{m}$ . Before installing the cavity in the vacuum chamber, the  $x$  and  $y$  lattice beams were carefully aligned to overlap with an uncertainty of  $\sim 3 \mu\text{m}$  measured with the knife-edge method.

Figure 1(d) shows the gravito-optical potentials for the cavity-enhanced optical lattice in the  $y$  direction at the atom loading position  $x_0$  with a peak intensity of  $I_L = 160 \text{ kW/cm}^2$ . The potential depends on the electronic states of the atoms and the lattice laser polarization. The gravitational potential energy  $mgy$  reduces the radial confinement of atoms in the optical lattice and determines the effective potential depth  $U_{\text{eff}}$ . For the lattice laser wavelength  $\lambda_L = 813 \text{ nm}$  [45], which is called the “magic wavelength,” the effective potential depths  $U_{\text{eff}}/k_B \approx 75 \mu\text{K}$  (indicated by the red line) become equal for the  $^1S_0$  and  $^3P_0$  states. For the  $^3P_2$  ( $m_J = 2$ ) state, the potential depth varies in the range of  $U_{\text{eff}}/k_B \approx 35\text{--}125 \mu\text{K}$ , depending on the lattice laser polarization angle  $\theta$  relative to the quantization axis.

### C. Pumping lasers

Atoms are loaded from the magnetic trap and transported by the moving lattice in the (i)  $^3P_2$ , (ii)  $^3P_0$ , or (iii)  $^1S_0$  states by applying pumping lasers. The pumping lasers also prevent the optical pumping of atoms induced by the optical lattice with the peak intensity of  $I_L = 160 \text{ kW/cm}^2$ , which causes the Raman transitions among the  $^3P_2$  and  $^3P_0$  metastable states, and the  $^1S_0$  ground state. For atoms in the  $^3P_2$  state, the excitation rate to the  $^3S_1$  state is estimated to be  $\sim 1.4 \text{ s}^{-1}$ .

(i) To transport atoms in the  $^3P_2$  state, we apply optical pumping lasers at 679 and 688 nm, respectively resonant to the  $^3P_0\text{--}^3S_1$  and  $^3P_1\text{--}^3S_1$  transitions [see Fig. 1(c)] along the moving lattice to prevent atoms from decaying to states other than the  $^3P_2$  state by the lattice-induced Raman transition.

(ii) To transport atoms in the  $^3P_0$  state, the magnetically trapped atoms in the  $^3P_2$  state are optically pumped to the  $^3S_1$  state by applying a 707 nm pumping laser [40,41]. We also apply a 688 nm pumping laser to prevent the atoms from decaying to the  $^1S_0$  state via the  $^3P_1$  state.

(iii) Atoms are pumped to the  $^1S_0$  state by turning off the MOT lasers at 461 nm and by applying both 707 and 679 nm pumping lasers. In this mode of operation, magnetically trapped atoms in the  $^3P_2$  state serve as an atom source that lasts a few seconds.

### D. Atom imaging and measurement sequence

Atoms are transported over 20 mm by the moving optical lattice to reach the observation region indicated by the small yellow square in Fig. 1(a), where atoms are imaged by applying a probe laser at 461 nm resonant to the  $^1S_0\text{--}^1P_1$  transition. In the cases when atoms are transported in the  $^3P_0$  or  $^3P_2$  states, we optically pump the atoms to the  $^1S_0$  state by switching the pumping lasers before the imaging. Figure 1(b) shows a fluorescence image of atoms taken by an electron-multiplying charge-coupled device (EMCCD) camera near the intersection region of  $3.5 \times 3.5 \text{ mm}^2$  with an exposure time of  $50 \mu\text{s}$ . The number of atoms  $N_A$  ( $N_B$ ) in box A (B), which is before (after) the intersection, is used to investigate the atom flux  $\phi$  and the transfer efficiency  $\kappa = N_B/N_A$  from the  $x$  lattice to the  $y$  lattice.

## III. RESULTS AND DISCUSSION

### A. Outcoupling of magnetically trapped atoms

Figure 3 shows the number of atoms that have traveled 20 mm from the magnetic trap as a function of the lattice velocity  $v_L$ . We measured the number of atoms  $N_A$  in box A along the  $x$  lattice [see Fig. 1(b)], where the atoms were in the  $^3P_0$  (red circles),  $^3P_2$  (green squares), and  $^1S_0$  (blue triangles) states. We set the lattice laser polarization  $\mathbf{E}_L^{(\perp)}$  perpendicular to the cavity plane [see Fig. 1(a)], which

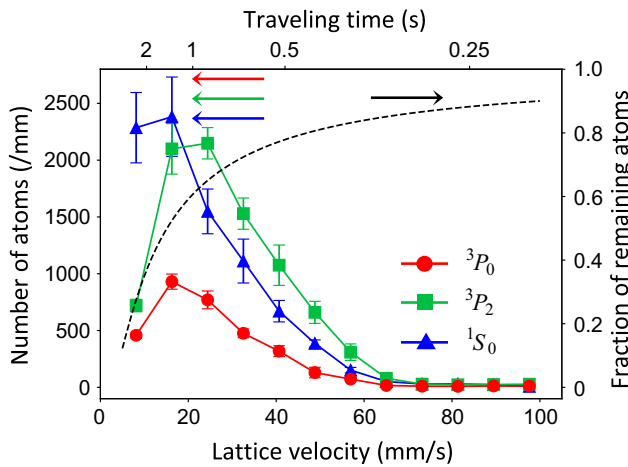


FIG. 3. Number of atoms in the  ${}^3P_0$  (red circles),  ${}^3P_2$  (green squares), and  ${}^1S_0$  (blue triangles) states outcoupled by the moving lattice with velocities  $v_L$ . The upper axis corresponds to the traveling time  $t$  of atoms over 20 mm, where the dashed line shows the fraction of remaining atoms, assuming the collision-limited lifetime of  $\tau = 2$  s.

gives 125- $\mu\text{K}$ -deep lattice potential for atoms in the  ${}^3P_2$  state at the loading position  $x_0$ .

The atoms pumped to the  ${}^3P_2$  and  ${}^3P_0$  states are continuously outcoupled with a maximum atom flux of  $\phi_{{}^3P_2} = 5 \times 10^4/\text{s}$  and  $\phi_{{}^3P_0} = 2 \times 10^4/\text{s}$ , respectively, for  $v_L \approx 20 \text{ mm/s}$ . This atom flux is an order of magnitude larger than that observed in our previous work [41], mainly because of a five times larger lattice laser radius while keeping a similar lattice depth, thanks to the power-buildup cavity. The atoms pumped to the  ${}^1S_0$  states are outcoupled from the magnetic trap by turning off the MOT lasers at 461 nm. The atom flux is  $\phi_{{}^1S_0} = 4 \times 10^4/\text{s}$ . Note that the outcoupling of atoms in the  ${}^1S_0$  state is not continuous.

The number of atoms decreases to zero as the lattice velocity approaches  $v_0 \approx 60 \text{ mm/s}$ , which is explained as follows. When the IR-cooled atoms in the  ${}^3P_2$  ( $m_J = 2$ ) state are loaded into the moving lattice at  $v_L$ , the atoms acquire kinetic energy of  $mv_L^2/2$ . For the atoms to be stably trapped in the lattice,  $mv_L^2/2 < U_{\text{eff}}/\eta$  needs to be satisfied, with  $\eta$  being the truncation factor [46]. The effective trap depth  $U_{\text{eff}}/k_B = 125 \mu\text{K}$  for the atoms in the  ${}^3P_2$  ( $m_J = 2$ ) state with the truncation factor  $\eta \approx 7$  reasonably accounts for the maximum velocity ( $v_0 \approx 60 \text{ mm/s}$ ) that corresponds to  $mv_0^2/(2k_B) \approx 20 \mu\text{K}$ . This truncation factor is also supported by the radial temperature 15  $\mu\text{K}$  of the transported atoms, as indicated by green squares in Fig. 5(c).

On the other hand, the number of transported atoms decreases for low lattice velocity  $v_1 < 20 \text{ mm/s}$ , which is attributed to the collisional loss of atoms during a long traveling time of  $t \approx 20 \text{ mm}/v_1 > 1 \text{ s}$ . Assuming the background-gas collision-limited lifetime of 2 s for atoms

in the optical lattice at  $10^{-7} \text{ Pa}$ , we estimate the fraction of remaining atoms as shown by the dashed line referring to the right axis in Fig. 3. In particular, for atoms in the  ${}^3P_0$  and  ${}^3P_2$  metastable states, energy pooling and light-assisted collisions [47] with the IR cooling laser may further reduce the lifetime.

## B. Crossed moving lattice

### 1. Atom transfer between the lattices and laser cooling

We expect the atoms in the  $x$ -moving lattice to be transferred to the  $y$ -moving lattice where the orthogonal moving lattices intersect, as the atoms follow the intensity maxima created by the interference or the sum of two moving lattice fields, as illustrated in Fig. 2. In the intersection, the atoms are guided by the lattice moving with the velocity  $\mathbf{v} = (v_L, v_L)$ , as indicated by the atom trajectories shown in Figs. 1(b) and 4. As the speed of the atoms is increased by  $\sqrt{2}$ , the atom density is reduced by  $\sqrt{2}$ , which explains the weaker fluorescence intensity in the intersection region.

We loaded atoms from the magnetic trap by the  $x$  lattice with the velocity  $v_m = 16 \text{ mm/s}$  to maximize the atom number, as indicated in Fig. 3. The trajectories of atoms traveling in the crossed moving lattice are summarized in Fig. 4, where atoms were pumped to the  ${}^3P_0$ ,  ${}^3P_2$ , and  ${}^1S_0$  states. Note that the atoms in the  ${}^3P_0$  and  ${}^3P_2$  states can coexist with the MOT lasers at 461 nm, allowing a fully continuous lattice-trapped atomic beam.

Using atoms pumped to the  ${}^1S_0$  state, we demonstrate laser cooling on the  ${}^1S_0-{}^3P_1$  transition to improve the transfer efficiency, as shown in Figs. 4(d) and 4(h). The cooling laser at 689 nm with a diameter of 10 mm illuminates the crossed region as depicted in Fig. 1(a). The laser is red-detuned from the light-shifted  ${}^1S_0-{}^3P_1$  ( $m_J = 0$ ) transition with an intensity of about 10 times the saturation intensity, i.e.,  $s \approx 10$ . We note that the  $m_J = \pm 1$  substates are off-resonant by more than 20 MHz because of the residual MOT magnetic field of about 1 mT. The capture velocity of the cooling transition [48] is given by  $v_c = \sqrt{s} \gamma_R/k_R \approx$

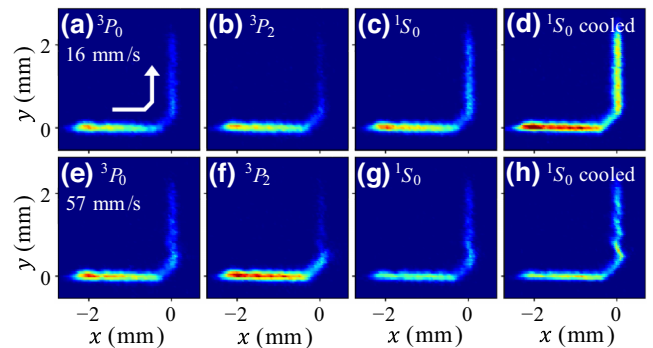


FIG. 4. Fluorescence images of atoms in the  ${}^3P_0$ ,  ${}^3P_2$ , and  ${}^1S_0$  states for lattice velocities of  $v_L = 16 \text{ mm/s}$  (upper row) and  $v_L = 57 \text{ mm/s}$  (lower row).

15 mm/s with  $\gamma_R = 7.5$  kHz being the natural linewidth and  $k_R$  the wavenumber of the transition.

For the moving lattice velocity  $v_L = 16$  mm/s, we measured the number of atoms along the atom trajectory [see black dotted line in Fig. 1(b)] and estimated the atom flux  $\phi$  as a function of the traveling time of the atoms, as shown in Fig. 5(a). In the absence of laser cooling, the atom flux decayed nonexponentially, especially after being transported to the  $y$  lattice, because of the heating of atoms in the transfer between the orthogonal lattices. In contrast, a nearly constant atom flux of  $\phi|_{S_0} = 6 \times 10^4$ /s was observed when applying laser cooling.

## 2. Velocity-dependent transfer

Figure 5(b) shows the velocity-dependent lattice transfer efficiency  $\kappa = N_B/N_A$  from the  $x$  lattice to the  $y$  lattice. We linearly increased (or decreased) the lattice velocity from  $v_m = 16$  mm/s to  $v_L$  in 100 ms before reaching  $x = -5$  mm. Figures 4(e)–4(h) show the atoms around the intersection with  $v_L = 57$  mm/s.

In the absence of laser cooling, transfer efficiencies  $\kappa = 0.3$ – $0.4$  were observed for  $v_L < 60$  mm/s for atoms in the  $^3P_0$  (red circles) and  $^1S_0$  (blue triangles) states. It is noticeable that the application of laser cooling around the intersection (purple stars) improved the transfer efficiency  $\kappa \approx 1$  for  $v_L < 10$  mm/s, which is comparable to the capture velocity  $v_c$  as given previously. Further decrease in the transfer efficiency for larger  $v_L$  may be attributed to the insufficient cooling for the larger kinetic energy  $mv_L^2/2$ , since the local light shift ( $> 1$  MHz) in the crossed region  $w \sim 200$   $\mu\text{m}$  limits the cooling time  $\sim w/v_L$  as  $v_L$  increases.

On the other hand, we observed low transfer efficiency  $\kappa < 0.1$  for atoms in the  $^3P_2$  state (green squares). We speculate that magnetic force acting on the magnetic moment  $3\mu_B$  of the  $^3P_2$  ( $m_J = 2$ ) state pushes the atoms out of the lattice while they are guided in the  $y$  lattice, where a magnetic field gradient  $|d\mathbf{B}/dx| \sim 2$  mT/cm reduces the effective lattice depth to  $\sim 30$   $\mu\text{K}$ . Here  $\mu_B$  is the Bohr magneton. We focus on the atom transport in the  $^3P_0$  and  $^1S_0$  states to simplify the following discussion without extra complication due to such magnetic forces.

## 3. Atomic temperature

We measured the temperature of lattice-trapped atoms by the time-of-flight technique. After optically pumping the atoms to the  $^1S_0$  state and turning off the lattice lasers, atoms were imaged by the 461-nm probe laser after a flight time of 5 ms. Figure 5(c) shows the radial temperatures of atoms before (filled symbols) and after (empty symbols) the intersection region as a function of the lattice velocity. We found that the atom temperatures of 10–20  $\mu\text{K}$  were rather independent of the velocity and the electronic states, as indicated by the different colors. The temperature of the atoms in the  $^3P_2$  state after the intersection is not shown in the figure as the lattice trap was unstable, as suggested by the rapid atom decay (green line) in Fig. 5(a).

The temperature of IR-cooled atoms in the magnetic trap is estimated to be  $T_{\text{eq}} \approx 84$   $\mu\text{K}$  for our saturation parameter  $s_{\text{IR}} = I_{\text{IR}}/I_0 \sim 6 \times 10^2$  and magnetic field gradient  $\beta_0 \approx 2$  mT/cm. Here we use the formula [41,49]

$$T_{\text{eq}} = (2T_D/3) \times s_{\text{IR}} / (2f_0 \sqrt{s_{\text{IR}}/f_0 - 1})$$

with  $f_0 = -(3\mu_B\beta_0 + mg)/(\hbar k_{\text{IR}}\gamma_{\text{IR}}/2)$ , where  $\gamma_{\text{IR}}/(2\pi) = 57$  kHz is the linewidth of the IR transition,

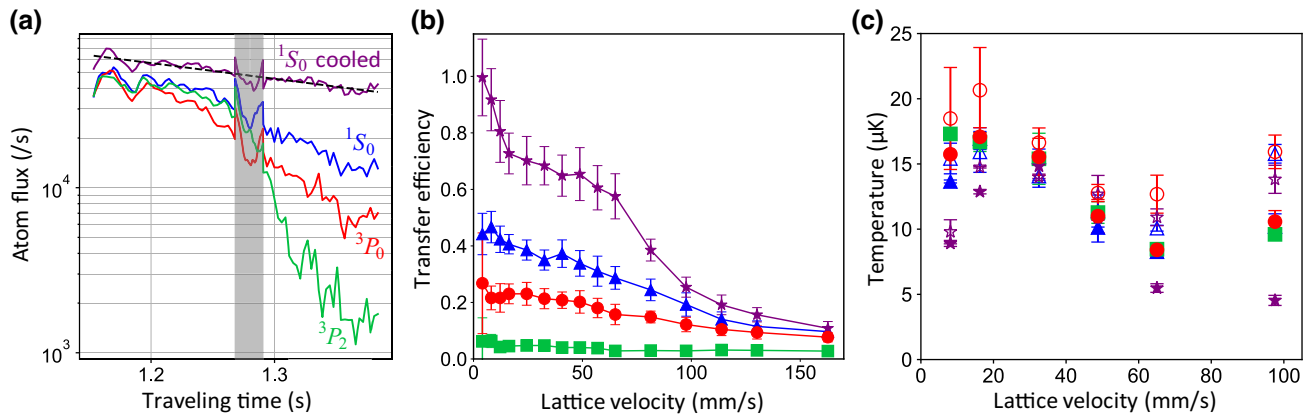


FIG. 5. (a) Atom flux as a function of the traveling time from the loading position  $x_0$  with  $v_L = 16$  mm/s. Atoms pass through the intersection at  $t = 1.268$ – $1.291$  s shown by the grey region. Different colors correspond to the atomic states, i.e.,  $^3P_0$  (red),  $^3P_2$  (green),  $^1S_0$  (blue), and  $^1S_0$  with the additional cooling (purple). The colors also apply to the following panels. Atom flux  $\phi = 6 \times 10^4$ /s is observed for atoms in the ground state when applying laser cooling. (b) Lattice velocity-dependent transfer efficiencies. Application of laser cooling (purple stars) improves the transfer efficiencies to unity for  $v_L < 10$  mm/s. (c) Temperatures of atoms before (filled symbols) and after (empty symbols) the intersection as a function of the lattice velocity.

$k_{\text{IR}} = 2\pi/\lambda_{\text{IR}}$  is the wavenumber, and  $T_D = \hbar\gamma_{\text{IR}}/(2k_B) = 1.4 \mu\text{K}$  is the Doppler temperature.

The effective lattice depth  $U_{\text{eff}}$  with the truncation factor of  $\eta = 7$  may account for the atom temperature  $U_{\text{eff}}/k_B/\eta \approx 10\text{--}14 \mu\text{K}$ . For atoms with energies larger than  $U_{\text{eff}}/\eta$ , the transfer efficiencies are less than  $\kappa = 0.4$  because of the heating of atoms at the intersection.

#### 4. Oscillatory motion of atoms

For the lattice velocity  $v_L = 57 \text{ mm/s}$ , we observe the radial oscillation motion of atoms within the lattice trap after it passes through the intersection, as shown in Fig. 4(h). Its spatial period of  $\Lambda \approx 0.59 \text{ mm}$  implies an oscillation frequency  $\Omega/(2\pi) = v_L/\Lambda \approx 100 \text{ Hz}$ , which agrees with the estimated radial trap frequency  $\Omega_L/(2\pi) = 125 \text{ Hz}$ . The observed amplitude  $A \approx 90 \mu\text{m}$  and the radial frequency suggest the maximum velocity of atoms in the harmonic oscillator to be  $v_M = A\Omega \approx 57 \text{ mm/s}$ , which is consistent with the lattice velocity.

The oscillation of the atomic trajectory suggests the following atom transfer mechanism between the moving lattices. The atoms in the  $x$  lattice with the potential depth  $u_0$  are guided by the four times deeper lattice  $4u_0$  created by the interference of the  $x$  and  $y$  lattices. In the intersection, atoms are accelerated to  $v_y = v_L$  and finally released to the  $y$ -moving lattice with  $x$  velocity  $v_x = v_L$ . When exiting the intersection, the atoms, therefore, gain kinetic energy of  $u_{\text{KE}} = mv_y^2/2 + mv_x^2/2 = mv_L^2$  in addition to the initial temperature  $k_B T_0$  of the atoms in the  $x$  lattice. This heating  $u_{\text{KE}}$  causes atom loss, as the atom temperature is given by the truncation of the  $y$  lattice  $T_0 \approx U_{\text{eff}}/k_B/\eta \approx 8 \mu\text{K}$ . Adiabatic deformation between the axial and radial confinements seems unfeasible, as the axial  $\omega_L/(2\pi) \approx 140 \text{ kHz}$  and radial  $\Omega_L/(2\pi) \approx 125 \text{ Hz}$  trap frequencies changed in a short transit time of milliseconds.

#### 5. Lattice polarization dependence

By setting the lattice polarization  $E_L^{(\parallel)}$  parallel to the cavity plane, as illustrated in Fig. 2(b), atoms tend to go straight rather than changing their direction as the lattice velocity increases. Figures 6(a) and 6(b) show the atoms in the  ${}^3P_0$  state with lattice velocities  $v_L = 16$  and  $97 \text{ mm/s}$ , respectively. The likelihood of capturing atoms in the  $y$  lattice decreases for  $v_L > 60 \text{ mm/s}$  because of the lack of interference between the crossed lattices. The fraction of atoms changing direction (filled circles) and going straight (empty circles) is summarized in Fig. 6(c) as a function of lattice velocity  $v_L$ . The rest of the atoms are lost from the lattice in the intersection region, as discussed below.

#### C. Trajectory simulation near the intersection

We simulated the classical trajectory of atoms in the  ${}^3P_0$  and  ${}^1S_0$  states with the Monte Carlo method. The

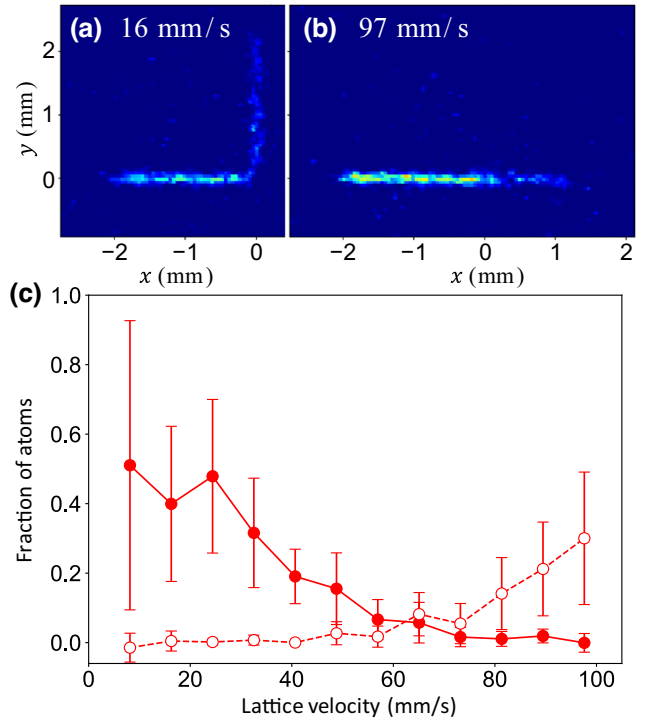


FIG. 6. Trajectory of atoms for the moving lattice with polarization  $E_L^{(\parallel)}$  parallel to the cavity plane. (a) Atoms partially change their direction for  $v_L = 16 \text{ mm/s}$ . (b) Atoms move along the  $x$  lattice for  $v_L = 97 \text{ mm/s}$ . (c) Fraction of atoms transitioning to the right-angle trajectory (filled circles) versus maintaining a straight path (empty circles).

equation of motion for an atom at  $\mathbf{r}(t)$  is given by  $m\ddot{\mathbf{r}}(t) = -\nabla U(\mathbf{r}, t)$ , where  $U(\mathbf{r}, t) = mgy - U_1|\bar{\mathbf{e}}(\mathbf{r}, t)|^2$  consists of the gravitational potential and the moving lattice potential, with  $m$  the atomic mass,  $g = 9.8 \text{ m/s}^2$  the gravitational acceleration, and  $U_1$  the lattice potential depth. The squared electric field  $|\bar{\mathbf{e}}(\mathbf{r}, t)|^2$  averaged over optical oscillation periods is given by

$$\begin{aligned} |\bar{\mathbf{e}}(\mathbf{r}, t)|^2 = & |\mathbf{e}_x|^2[1 + \cos(2kx - \Delta\omega t)] \\ & + |\mathbf{e}_y|^2[1 + \cos(2ky - \Delta\omega t)] \\ & + 2|\mathbf{e}_x \cdot \mathbf{e}_y|[\cos(k(x - y)) \\ & + \cos(k(x + y) - \Delta\omega t)], \end{aligned} \quad (1)$$

where  $\mathbf{e}_{x(y)}$  is the normalized electric field for one of the counterpropagating moving lattice lasers along the  $x(y)$  axis with the wave number  $k = 2\pi/\lambda_L$  and the angular-frequency difference  $\Delta\omega = 2\pi\Delta\nu$  of the counterpropagating lattice lasers. The spatial distribution of the electric field is given by

$$\begin{aligned} \mathbf{e}_x(\mathbf{r}) = & \frac{1}{\sqrt{2}} \exp[-(z^2 + y^2)/w_1^2] \\ \mathbf{e}_y(\mathbf{r}) = & \frac{w_1}{\sqrt{2}w_2} \exp[-(z^2 + x^2)/w_2^2], \end{aligned}$$

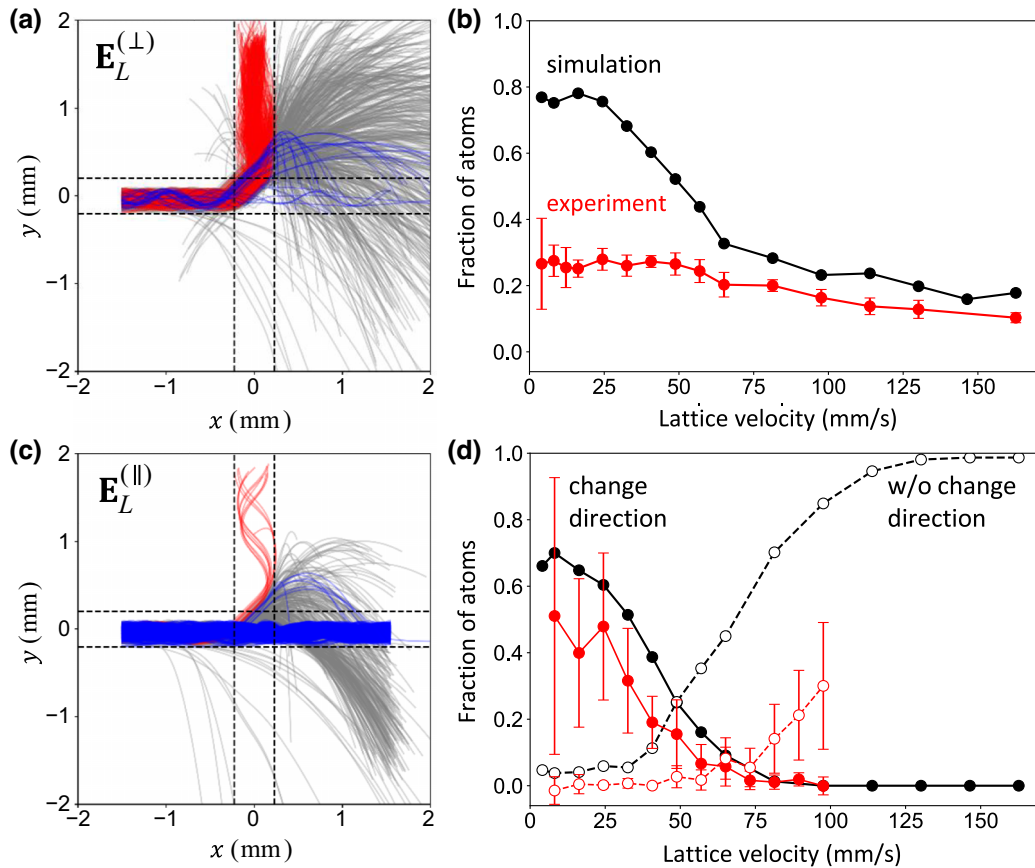


FIG. 7. (a),(c) Simulated atom trajectories for the two lattice polarizations: (a)  $\mathbf{E}_L^{(\perp)}$  and (c)  $\mathbf{E}_L^{(\parallel)}$ . Red, blue, and grey trajectories show the atoms changing direction, going straight, and being lost from the lattice, respectively. (b),(d) Fraction of atoms transitioning from the  $x$ -moving lattice to the  $y$ -moving lattice (filled circles) and remaining in the  $x$ -moving lattice (empty circles) for the two lattice polarizations: (b)  $\mathbf{E}_L^{(\perp)}$  and (d)  $\mathbf{E}_L^{(\parallel)}$ . Results of simulations are indicated by black symbols. The interference term  $|\mathbf{e}_x \cdot \mathbf{e}_y| \neq 0$  facilitates transferring atoms from the  $x$  lattice to the  $y$  lattice for higher moving lattice velocity  $v_L > 60$  mm/s. Experimental results for atoms in the  ${}^3P_0$  state are indicated by red symbols.

where  $w_1 = 203$   $\mu\text{m}$  and  $w_2 = 228$   $\mu\text{m}$  are the beam radii for the  $x$  and  $y$  lattices, respectively, as described earlier. We prepare atoms in the  $x$  lattice at  $x = -1.5$  mm, assuming thermal distribution with  $T_1 = 10$   $\mu\text{K}$  in the truncated harmonic trap with  $U_1/k_B = 70$   $\mu\text{K}$ . We integrate the differential equation using the leapfrog method.

For the lattice laser polarization perpendicular to the cavity plane  $\mathbf{e}_x \parallel \mathbf{e}_y \parallel \hat{\mathbf{z}}$ , the inter-axis constructive interference  $|\mathbf{e}_x \cdot \mathbf{e}_y| \neq 0$  facilitates guiding of atoms toward  $45^\circ$  with respect to the  $x$  axis at the intersection region. Figure 7(a) shows the simulated trajectories for  $v_L = 80$  mm/s for  $10^3$  atoms. Figure 7(b) shows the fraction of atoms transitioning from the  $x$  lattice to the  $y$  lattice calculated from the trajectories shown in red in Fig. 7(a). The simulations reproduce the atom transport between the orthogonal lattices. A factor of 2 discrepancy between the experiments and simulations may be attributed to the extra heating of lattice-trapped atoms in the experiment, such as given by laser-noise-induced parametric heating, which may cause a loss of atoms.

For the lattice laser polarization parallel to the cavity plane, the disappearance of the interference term ( $|\mathbf{e}_x \cdot \mathbf{e}_y| = 0$ ) makes the redirecting of atoms less effective for atoms with  $v_L > 60$  mm/s. Figure 7(c) shows the atom trajectories for  $v_L = 80$  mm/s, which indicates that a large fraction of atoms go straight (blue trajectories). Atoms lost from the lattice are shown by grey trajectories, and those transported to the  $y$  lattice are shown by red ones. Figure 7(d) summarizes the transfer efficiencies, where filled circles show the fraction of atoms transported to the  $y$  lattice, and empty circles show the atoms that remain trapped in the  $x$  lattice. The simulations shown in black reproduce the velocity-dependent trend observed in the experiments (red circles) taken from Fig. 6(c).

#### IV. CONCLUSION

We have demonstrated a continuous beam of strontium atoms in the  ${}^3P_0$  and  ${}^3P_2$  metastable states while the two-stage cooling is being conducted. The interference of two

moving lattices facilitates the guiding of the atoms to the orthogonal moving lattice, where atoms can be free from the scattered light in laser cooling. The obtained atom flux of  $\phi > 10^4/\text{s}$  is sufficient for longitudinal Ramsey spectroscopy [43]. The scheme has been extended to  $^{87}\text{Sr}$  to obtain an atom flux of one-tenth of  $^{88}\text{Sr}$ , which is roughly proportional to the natural abundance of the isotopes, by following the narrow-line cooling on  $^{87}\text{Sr}$  as reported earlier [38]. A continuous beam of atoms trapped in the LDR provides an essential resource for longitudinal spectroscopy, where atoms in the LDR interact with a probe laser introduced in the same axis as the lattice-trapped atomic beam. The configuration allows zero-dead-time spectroscopy free from the Doppler shift arising from the thermal motion of atoms.

While we observed the loss of atoms in transferring between the orthogonal moving lattices, we demonstrated that laser cooling of atoms improves the transfer efficiency close to unity. For the continuous clock operation on the  $^1\text{S}_0 - ^3\text{P}_0$  transition, laser cooling on the  $^3\text{P}_2 - ^3\text{D}_3$  transition at  $\lambda = 2.92 \mu\text{m}$  can be applied in the intersection region to improve the transfer efficiency. This laser cooling can be compatible with the clock operation, as it gives a negligible light shift at  $10^{-20}$  level [38] on the clock transition.

## ACKNOWLEDGMENTS

We thank M. Takamoto for experimental support, H. Chiba for assistance in experiments, and C.-C. Chen for careful reading of the manuscript and useful comments. This work received support from the Japan Science and Technology Agency (JST) Mirai Program Grant No. JPMJMI18A1.

- [1] T. M. Graham *et al.*, Multi-qubit entanglement and algorithms on a neutral-atom quantum computer, *Nature* **604**, 457 (2022).
- [2] D. Bluvstein *et al.*, Logical quantum processor based on reconfigurable atom arrays, *Nature* **626**, 58 (2023).
- [3] R. Islam, R. Ma, P. M. Preiss, M. E. Tai, A. Lukin, M. Rispoli, and M. Greiner, Measuring entanglement entropy in a quantum many-body system, *Nature* **528**, 77 (2015).
- [4] C. Gross and I. Bloch, Quantum simulations with ultracold atoms in optical lattices, *Science* **357**, 995 (2017).
- [5] F. Schäfer, T. Fukuhara, S. Sugawa, Y. Takasu, and Y. Takahashi, Tools for quantum simulation with ultracold atoms in optical lattices, *Nat. Rev. Phys.* **2**, 411 (2020).
- [6] P. Scholl, M. Schuler, H. J. Williams, A. A. Eberharter, D. Barredo, K.-N. Schymik, V. Lienhard, L.-P. Henry, T. C. Lang, T. Lahaye, A. M. Läuchli, and A. Browaeys, Quantum simulation of 2D antiferromagnets with hundreds of rydberg atoms, *Nature* **595**, 233 (2021).
- [7] B. J. Bloom, T. L. Nicholson, J. R. Williams, S. L. Campbell, M. Bishop, X. Zhang, W. Zhang, S. L. Bromley, and J. Ye, An optical lattice clock with accuracy and stability at the  $10^{-18}$  level, *Nature* **506**, 71 (2014).
- [8] I. Ushijima, M. Takamoto, M. Das, T. Ohkubo, and H. Katori, Cryogenic optical lattice clocks, *Nat. Photonics* **9**, 185 (2015).
- [9] M. A. Norcia, M. N. Winchester, J. R. Cline, and J. K. Thompson, Superradiance on the millihertz linewidth strontium clock transition, *Sci. Adv.* **2**, e1601231 (2016).
- [10] M. Schioppo, R. C. Brown, W. F. McGrew, N. Hinkley, R. J. Fasano, K. Beloy, T. H. Yoon, G. Milani, D. Nicolodi, J. A. Sherman, N. B. Phillips, C. W. Oates, and A. D. Ludlow, Ultrastable optical clock with two cold-atom ensembles, *Nat. Photonics* **11**, 48 (2017).
- [11] M. Kasevich and S. Chu, Atomic Interferometry Using Stimulated Raman Transitions, *Phys. Rev. Lett.* **67**, 181 (1991).
- [12] F. Riehle, T. Kisters, A. Witte, J. Helmcke, and C. J. Borde, Optical Ramsey Spectroscopy in a Rotating Frame: Sagnac Effect in a Matter-Wave Interferometer, *Phys. Rev. Lett.* **67**, 177 (1991).
- [13] D. S. Durfee, Y. K. Shaham, and M. A. Kasevich, Long-Term Stability of an Area-Reversible Atom-Interferometer Sagnac Gyroscope, *Phys. Rev. Lett.* **97**, 240801 (2006).
- [14] G. Rosi, F. Sorrentino, L. Cacciapuoti, M. Prevedelli, and G. M. Tino, Precision measurement of the Newtonian gravitational constant using cold atoms, *Nature* **510**, 518 (2014).
- [15] I. Dutta, D. Savoie, B. Fang, B. Venon, C. L. Garrido Alzar, R. Geiger, and A. Landragin, Continuous Cold-Atom Inertial Sensor with 1 nrad/sec Rotation Stability, *Phys. Rev. Lett.* **116**, 183003 (2016).
- [16] G. J. Dick, in *Proceedings of the 19th Annual Precise Time and Time Interval Systems and Applications Meeting, Redondo Beach, 1987*, (U.S. Naval Observatory, Washington, DC, 1988), p. 133.
- [17] W. M. Itano, J. C. Bergquist, J. J. Bollinger, J. M. Gilligan, D. J. Heinzen, F. L. Moore, M. G. Raizen, and D. J. Wineland, Quantum projection noise: Population fluctuations in two-level systems, *Phys. Rev. A* **47**, 3554 (1993).
- [18] G. W. Biedermann, K. Takase, X. Wu, L. Deslauriers, S. Roy, and M. A. Kasevich, Zero-Dead-Time Operation of Interleaved Atomic Clocks, *Phys. Rev. Lett.* **111**, 170802 (2013).
- [19] L. Essen and J. V. L. Parry, An atomic standard of frequency and time interval: A caesium resonator, *Nature* **176**, 280 (1955).
- [20] J. Olson, R. W. Fox, T. M. Fortier, T. F. Sheerin, R. C. Brown, H. Leopardi, R. E. Stoner, C. W. Oates, and A. D. Ludlow, Ramsey-Bordé Matter-Wave Interferometry for Laser Frequency Stabilization at  $10^{-16}$  Frequency Instability and Below, *Phys. Rev. Lett.* **123**, 073202 (2019).
- [21] P. Berthoud, A. Joyet, G. Dudle, N. Sagna, and P. Thomann, A continuous beam of slow, cold cesium atoms magnetically extracted from a 2D magneto-optical trap, *Euro. Phys. Lett.* **41**, 141 (1998).
- [22] J. M. Kwolek and A. T. Black, Continuous sub-Doppler-cooled atomic beam interferometer for inertial sensing, *Phys. Rev. Appl.* **17**, 024061 (2022).
- [23] C.-C. Chen, R. González Escudero, J. Minář, B. Pasquiou, S. Bennetts, and F. Schreck, Continuous Bose-Einstein condensation, *Nature* **606**, 683 (2022).

- [24] R. Grimm, M. Weidemüller, and Y. B. Ovchinnikov, *Optical Dipole Traps for Neutral Atoms* (Academic Press, Cambridge, Massachusetts, 2000), p. 95.
- [25] C.-C. Chen, S. Bennetts, R. G. Escudero, B. Pasquiou, and F. Schreck, Continuous guided strontium beam with high phase-space density, *Phys. Rev. Appl.* **12**, 044014 (2019).
- [26] E. A. Hinds and I. G. Hughes, Magnetic atom optics: Mirrors, guides, traps, and chips for atoms, *J. Phys. D: Appl. Phys.* **32**, R119 (1999).
- [27] D. Müller, D. Z. Anderson, R. J. Grow, P. D. D. Schwindt, and E. A. Cornell, Guiding Neutral Atoms Around Curves with Lithographically Patterned Current-Carrying Wires, *Phys. Rev. Lett.* **83**, 5194 (1999).
- [28] R. Folman, P. Krüger, J. Schmiedmayer, J. Denschlag, and C. Henkel, Microscopic atom optics: From wires to an atom chip, *Adv. At. Mol. Opt. Phys.* **48**, 263 (2002).
- [29] W. Hänsel, J. Reichel, P. Hommelhoff, and T. W. Hänsch, Magnetic Conveyor Belt for Transporting and Merging Trapped Atom Clouds, *Phys. Rev. Lett.* **86**, 608 (2001).
- [30] H. Ott, J. Fortagh, G. Schlotterbeck, A. Grossmann, and C. Zimmermann, Bose-Einstein Condensation in a Surface Microtrap, *Phys. Rev. Lett.* **87**, 230401 (2001).
- [31] J. Beugnon, C. Tuchendler, H. Marion, A. Gaëtan, Y. Miroshnychenko, Y. R. P. Sortais, A. M. Lance, M. P. A. Jones, G. Messin, A. Browaeys, and P. Grangier, Two-dimensional transport and transfer of a single atomic qubit in optical tweezers, *Nat. Phys.* **3**, 696 (2007).
- [32] M. J. Renn, D. Montgomery, O. Vdovin, D. Z. Anderson, C. E. Wieman, and E. A. Cornell, Laser-Guided Atoms in Hollow-Core Optical Fibers, *Phys. Rev. Lett.* **75**, 3253 (1995).
- [33] S. Vorrath, S. A. Möller, P. Windpassinger, K. Bongs, and K. Sengstock, Efficient guiding of cold atoms through a photonic band gap fiber, *New J. Phys.* **12**, 123015 (2010).
- [34] S. Kuhr, W. Alt, D. Schrader, I. Dotsenko, Y. Miroshnychenko, W. Rosenfeld, M. Khudaverdyan, V. Gomer, A. Rauschenbeutel, and D. Meschede, Coherence Properties and Quantum State Transportation in an Optical Conveyor Belt, *Phys. Rev. Lett.* **91**, 213002 (2003).
- [35] S. Schmid, G. Thalhammer, K. Winkler, F. Lang, and J. Hecker Denschlag, Long distance transport of ultracold atoms using a 1D optical lattice, *New J. Phys.* **8**, 159 (2006).
- [36] T. Ido and H. Katori, Recoil-Free Spectroscopy of Neutral Sr Atoms in the Lamb-Dicke Regime, *Phys. Rev. Lett.* **91**, 053001 (2003).
- [37] R. Hobson, W. Bowden, A. Vianello, I. R. Hill, and P. Gill, Midinfrared magneto-optical trap of metastable strontium for an optical lattice clock, *Phys. Rev. A* **101**, 013420 (2020).
- [38] T. Akatsuka, K. Hashiguchi, T. Takahashi, N. Ohmae, M. Takamoto, and H. Katori, Three-stage laser cooling of Sr atoms using the  $5s5p\ ^3P_2$  metastable state below Doppler temperatures, *Phys. Rev. A* **103**, 023331 (2021).
- [39] H. Katori, T. Ido, Y. Isoya, and M. Kuwata-Gonokami, Laser cooling of strontium atoms toward quantum degeneracy, *AIP Conf. Proc.* **551**, 382 (2001).
- [40] C. Y. Yang, P. Halder, O. Appel, D. Hansen, and A. Hemmerich, Continuous loading of  $^1S_0$  calcium atoms into an optical dipole trap, *Phys. Rev. A* **76**, 033418 (2007).
- [41] R. Takeuchi, H. Chiba, S. Okaba, M. Takamoto, S. Tsuji, and H. Katori, Continuous outcoupling of ultracold strontium atoms combining three different traps, *Appl. Phys. Express* **16**, 042003 (2023).
- [42] Y. Miroshnychenko, W. Alt, I. Dotsenko, L. Förster, M. Khudaverdyan, D. Meschede, D. Schrader, and A. Rauschenbeutel, Quantum engineering: An atom-sorting machine, *Nature* **442**, 151 (2006).
- [43] H. Katori, Longitudinal Ramsey spectroscopy of atoms for continuous operation of optical clocks, *Appl. Phys. Express* **14**, 072006 (2021).
- [44] M. Yasuda and H. Katori, Lifetime Measurement of the  $^3P_2$  Metastable State of Strontium Atoms, *Phys. Rev. Lett.* **92**, 153004 (2004).
- [45] M. Takamoto and H. Katori, Spectroscopy of the  $^1S_0$ – $^3P_0$  Clock Transition of  $^{87}\text{Sr}$  in an Optical Lattice, *Phys. Rev. Lett.* **91**, 223001 (2003).
- [46] W. Ketterle and N. V. Druten, *Evaporative Cooling of Trapped Atoms* (Academic Press, Cambridge, Massachusetts, 1996), p. 181.
- [47] J. Weiner, V. S. Bagnato, S. Zilio, and P. S. Julienne, Experiments and theory in cold and ultracold collisions, *Rev. Mod. Phys.* **71**, 1 (1999).
- [48] H. Katori, T. Ido, Y. Isoya, and M. Kuwata-Gonokami, Magneto-Optical Trapping and Cooling of Strontium Atoms Down to the Photon Recoil Temperature, *Phys. Rev. Lett.* **82**, 1116 (1999).
- [49] A. J. Berglund, J. L. Hanssen, and J. J. McClelland, Narrow-Line Magneto-Optical Cooling and Trapping of Strongly Magnetic Atoms, *Phys. Rev. Lett.* **100**, 113002 (2008).